



In situ Lu–Hf geochronology of calcite

Alexander Simpson^{1,2}, Stijn Glorie^{1,2}, Martin Hand^{1,2}, Carl Spandler¹, Sarah Gilbert³, and Brad Cave¹

¹Department of Earth Sciences, School of Physical Sciences, The University of Adelaide, Adelaide SA-5005, Australia

²Mineral Exploration Cooperative Research Centre (MinEx CRC), The University of Adelaide, Adelaide SA-5005, Australia

³Adelaide Microscopy, The University of Adelaide, Adelaide SA-5005, Australia

Correspondence: Alexander Simpson (alexander.simpson@adelaide.edu.au)

Received: 23 December 2021 – Discussion started: 6 January 2022

Revised: 11 April 2022 – Accepted: 29 April 2022 – Published: 8 June 2022

Abstract. The ability to constrain the age of calcite formation is of great utility to the Earth science community, due to the ubiquity of calcite across a wide spectrum of geological systems. Here, we present the first in situ laser ablation inductively coupled tandem quadrupole mass spectrometry (LA-ICP-MS/MS) Lu–Hf ages for calcite, demonstrating geologically meaningful ages for iron oxide copper gold (IOCG) and skarn mineralisation, carbonatite intrusion, and low-grade metamorphism. The analysed samples range in age between ca. 0.9 and ca. 2 Ga with uncertainties between 1.7 % and 0.6 % obtained from calcite with Lu concentrations as low as ca. 0.5 ppm. The Lu–Hf system in calcite appears to be able to preserve primary precipitation ages over a significant amount of geological time, although further research is required to constrain the closure temperature. The in situ approach allows calcite to be rapidly dated while maintaining its petrogenetic context with mineralisation and other associated mineral processes. Therefore, LA-ICP-MS/MS Lu–Hf dating of calcite can be used to resolve the timing of complex mineral paragenetic sequences that are a feature of many ancient rock systems.

1 Introduction

Calcite (CaCO_3) is the main mineral phase of most carbonate sedimentary rocks and their metamorphic equivalents. Calcite is also a common diagenetic phase and is a major component of carbonatites. Calcite is also a common product of hydrothermal alteration and constituent of mineralising systems where it may precipitate from fluids during pre-ore, ore-stage, and post-ore forming processes (Debruyne et al., 2016). The ability to directly date calcite unlocks the possi-

bility of constraining the timing of a vast array of geological processes that can be difficult to date using conventional methods.

Accurate in situ U–Pb geochronology of calcite has been applied to a variety of geological systems (e.g. Li et al., 2014; Roberts and Walker, 2016; Ring and Gerdes, 2016). However, calcite often incorporates significant quantities of Pb during crystallisation (i.e. “initial” or “common” Pb), which can limit the utility of U–Pb geochronology (Rasbury and Cole, 2009). Moreover, Pb is highly fluid mobile (Brugger et al., 2016), so it can be difficult to obtain primary age information with the U–Pb method in hydrothermal or strongly altered systems (Roberts et al., 2020; Simpson et al., 2021b). Further, given the propensity for calcite to undergo recrystallisation, calcite U–Pb geochronology is rarely applicable to Precambrian systems as the calcite U–Pb system invariably does not remain closed over long timescales (Whitehouse and Russell, 1997).

Alternative dating systems involving the radioisotopic decay of rare earth elements (REEs) such as Sm–Nd and Lu–Hf, have previously been applied to calcite (e.g. Maas et al., 2020; Barker et al., 2009; Peng et al., 2003; Nie et al., 1999), based on the moderate to strong compatibility of REEs in carbonates in many systems (Debruyne et al., 2016; Zhong and Mucci, 1995; Terakado and Masuda, 1988; Elzinga et al., 2002). However, it should be noted that REE compatibility will be dependent on the conditions of calcite formation and can vary. Importantly for geochronology, experimental evidence indicates that Lu and Hf are highly immobile in many hydrothermal fluids (Migdisov et al., 2016; Brugger et al., 2016), meaning that the Lu–Hf system is potentially preserved relative to the U–Pb system during post-formation processes. However, concentrations of Lu and Hf are gener-

ally low (ppm to ppt range) in calcite, necessitating the dissolution of large quantities of material (up to 2 g) per sample for conventional Lu–Hf geochronology (Maas et al., 2020). These large quantities significantly reduce the spatial resolution of the technique and have the additional problem of potential contamination from inclusions. Furthermore, age variation is difficult to detect, and bulk samples may produce a meaningless average age derived from mixing of age domains. The dissolution process also removes calcite from its petrological context. The recent development of in situ Lu–Hf geochronology of individual minerals by laser ablation inductively coupled tandem quadrupole mass spectrometry (LA-ICP-MS/MS) allows for rapid acquisition of spatially resolved data, and has been demonstrated for garnet (Ribeiro et al., 2021; Tamblyn et al., 2021) and apatite (Glorie et al., 2022).

In this study, we present the first in situ Lu–Hf dating of calcite from a variety of geological environments. We demonstrate that in situ calcite Lu–Hf geochronology can produce meaningful ages for complexly deformed and hydrothermally altered systems, such as mineral deposits, as well as carbonatite intrusions and low-grade metamorphism.

2 Geological background of samples

The analysed samples were selected (1) to demonstrate that calcite Lu–Hf can date primary calcite formation in carbonatites, (2) to reveal the potential of the method to unravel complex ore systems or later events, and (3) to characterise large calcite samples that would make suitable reference materials for in situ analysis.

2.1 Phalaborwa carbonatite, South Africa

The Phalaborwa Igneous Complex is located ~450 km northeast of Johannesburg, in Limpopo Province, South Africa. The igneous complex is the result of several distinct pulses of alkaline intrusions that were emplaced into Archean granitic gneiss (Staff, 1976). The Loolekop pipe is located in the centre of the Phalaborwa Igneous Complex and was intruded by two episodes of carbonatite emplaced at the intersection of five major faults and shear zones (Staff, 1976; Basson et al., 2017). The oldest carbonatite is termed the “transgressive banded” carbonatite and has an emplacement age of 2060.0 ± 2.2 Ma (baddeleyite secondary ion mass spectrometry (SIMS) U–Pb; Wu et al., 2011). This is intruded by a slightly younger carbonatite termed the “banded” carbonatite and has an emplacement age of 2059.8 ± 1.3 Ma (baddeleyite SIMS U–Pb; Wu et al., 2011). The Phalaborwa carbonatite is unique as it is the only known example of a carbonatite containing economic Cu mineralisation (Groves and Vielreicher, 2001). In the banded carbonatite–phoscorite, Cu mineralisation is primarily in the form of bornite inter-grown with valleriite with minor chalcopyrite (Staff, 1976). In the transgressive car-

bonatite, Cu mineralisation is present as chalcopyrite inter-grown with cubanite and valleriite (Staff, 1976). Cu mineralisation is interpreted as being magmatic–hydrothermal in origin, with Cu leached by high-temperature hydrothermal fluids at depth, precipitating along fractures within the hosting carbonatite (Le Bras et al., 2021). The sample used in this study (P01) is representative of carbonatite-hosted Cu mineralisation from within the Loolekop pipe (Fig. 1). The sample is mineralogically composed of chalcopyrite inter-grown with cubanite and pyrrhotite alongside an assemblage of magnetite, dolomite, calcite, biotite, pyroxene, and valleriite. As the Phalaborwa carbonatite has a well-constrained crystallisation age, it provides an ideal case study to demonstrate the utility of the in situ Lu–Hf method for dating igneous calcite directly associated with Cu mineralisation.

2.2 The Eastern Fold Belt, Mt Isa Block, Queensland, Australia

The Eastern Fold Belt of the Mount Isa Domain has experienced multiple episodes of deformation, magmatism, metamorphism, mineralisation, and pervasive hydrothermal alteration across the Paleo- to Mesoproterozoic and hence represents one of the most metasomatised crustal blocks on Earth (Oliver et al., 2008). Hydrothermal calcite is common across the Mount Isa region, in the Mary Kathleen Domain (Oliver et al., 1993) and in many of the IOCG deposits of the Cloncurry District. For this study we have selected calcite samples from the Lime Creek calcite quarry and the Mt Elliott IOCG deposit for Lu–Hf analysis. The Mt Isa Domain has both regional and deposit-level age constraints, making it a good area to demonstrate the technique.

The Lime Creek quarry is one of a number of large calcite pods or veins that are exposed in Mary Kathleen Domain. The Lime Creek quarry is hosted within the ca. 1760 Ma Argylla Formation and lies along the steeply dipping NNW-trending Tribulation–Lime Creek Fault, which offsets regional-scale “D₂” folds (Marshall, 2003). Breccias along this fault contain clasts of calc–silicate rocks and metadiorite with a matrix consisting of albite–actinolite–diopside–biotite–titanite–apatite that are subsequently overprinted by the undeformed Lime Creek calcite-dominated veins (Marshall, 2003). These veins are extremely coarse-grained with calcite crystals larger than 1 m³, actinolite crystals over 1 m in length, and apatite, biotite, diopside, and titanite grains over 20 cm in diameter (Oliver et al., 1993; Marshall, 2003). Based on cross-cutting relationships, it is interpreted as the Lime Creek vein system and other calcite pods and veins of this style precipitating post-faulting during late-“D₃” deformation (ca. 1550–1500 Ma) of the Isan Orogeny (Giles and Nutman, 2002; Marshall, 2003). This style of veining is common throughout the Mary Kathleen Domain and provides evidence of kilometre-scale fluid transport during late-stage metamorphism (Oliver et al., 1993). Based on C and O isotope analysis of calcite from these

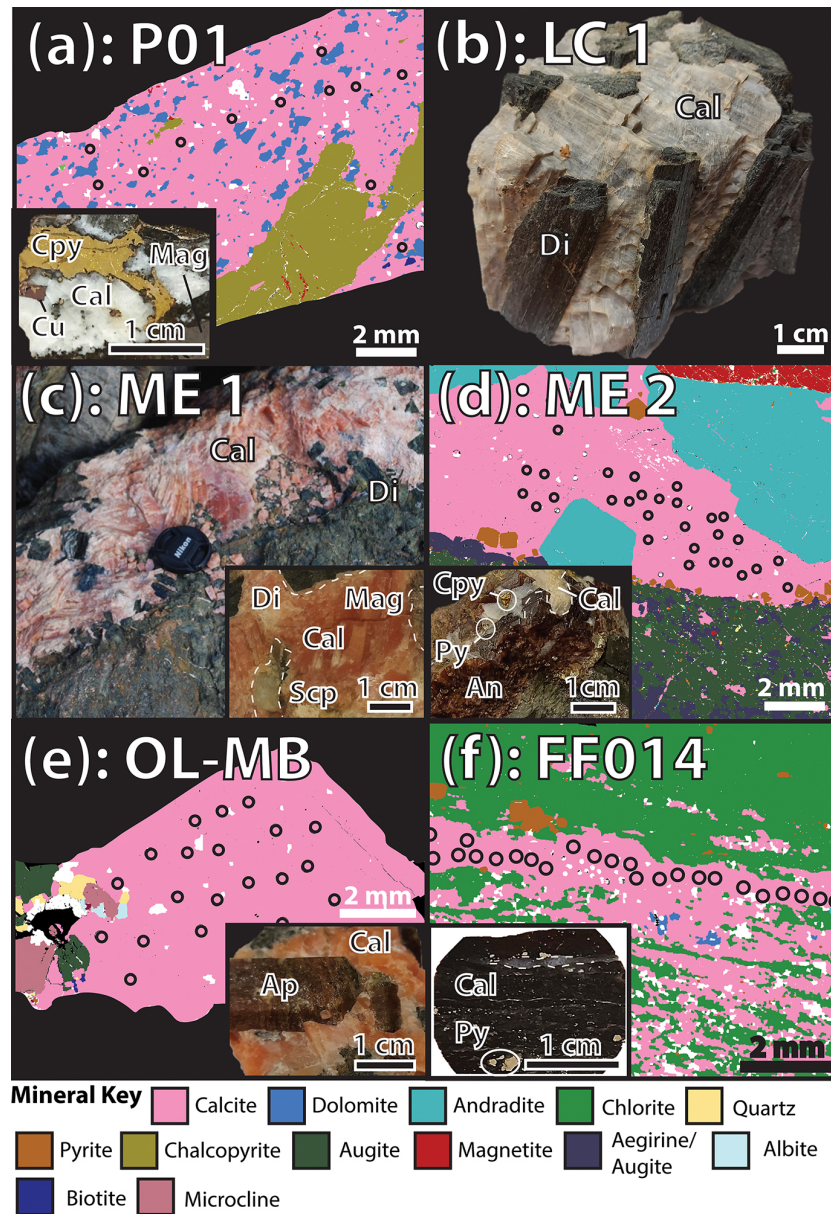


Figure 1. A combination of SEM mineral maps (a, c, d, e) and photos of analysed samples. (a) P01 (Phalaborwa carbonatite) shows calcite in petrogenetic context to chalcopyrite. (b) Photo of LC 1 hand sample. (c) Photo of the ME 1 sample in outcrop, with inset showing the mineralogy of the analysed sample. (d) Calcite from ME 2 (Mt Isa) in contact with hematite, pyrrhotite, and andradite, with inset showing hand sample. (e) OL-MB (Otter Lake), showing analysed calcite with associated minerals, with inset showing relationship between apatite (Ap) and calcite (Cal) in hand sample. (f) FF014 (Flin Flon deposit) shows calcite vein in chlorite matrix with disseminated pyrite, with inset showing analysed block (dark coloured matrix is composed of chlorite). Black circles represent laser spot locations. Mineral abbreviations: Cal – calcite; Cpy – chalcopyrite; Py – pyrite; Mag – magnetite; Cu – cubanite; Di – diopside; Scp – scapolite; An – andradite. Larger-size sample images are included in Appendix C.

veins, they are interpreted as having formed from hydrothermal fluids likely associated with the intrusion of the ca. 1530 to 1500 Ma Williams–Naraku batholiths (Oliver et al., 1993). Although no direct dating has been completed on the Lime Creek quarry, titanite from the nearby and cognate Knobby Quarry has produced three titanite U–Pb ages of 1521 ± 5 ,

1527 ± 7 , and 1555 ± 5 Ma (Oliver et al., 2004). The sample analysed in this study (LC1) consists of very coarse-grained calcite with coarse-grained diopside collected from a large calcite pod in the Lime Creek quarry (Fig. 1).

Mt Elliott is an IOCG deposit located in the Eastern Fold Belt of the Mount Isa Inlier (Duncan et al.,

2011). The deposit is situated within northwest-striking splays of the Mount Dore Fault (Wang and Williams, 2001; Duncan et al., 2011) and is hosted within skarn-altered and deformed phyllites and schists (Garrett, 1992; Wang and Williams, 2001). The host rocks were metamorphosed to lower amphibolite facies during the ca. 1600–1580 Ma D₂ deformation of the Isan Orogeny (Wang and Williams, 2001; Garrett, 1992). The formation of early albite–hematite (red rock) alteration enhanced brittle fracturing and brecciation of the shale (Garrett, 1992). This was infilled by two stages of open-space skarn development: (1) diopside–magnetite–hematite–calcite–titanite–allanite–phlogopite and (2) actinolite–scapolite–magnetite–andradite–calcite–epidote–allanite–chlorite and biotite (Garrett, 1992; Wang and Williams, 2001). Sulfides in the second stage include chalcopyrite, pyrrhotite, and pyrite (Garrett, 1992). Although the two skarn assemblages are difficult to distinguish mineralogically, the second episode is the most widespread and represents the major Cu–Au event (Garrett, 1992; Wang and Williams, 2001). A variety of geochronological techniques have been applied to constrain the age of Cu–Au mineralisation. The earliest phase of skarn development has been dated to 1530 ± 11 Ma (U–Pb titanite; Duncan et al., 2011). The second stage of skarn development associated with Cu–Au mineralisation has been dated to 1513 ± 5 Ma (molybdenite Re–Os; Duncan et al., 2011) and 1510 ± 3 Ma (actinolite Ar–Ar; Wang and Williams, 2001). Two outcrop samples from the Mount Elliott Cu–Au deposit were selected for Lu–Hf geochronology. Mt Elliott 1 (ME 1) consists of coarse-grained pink-coloured calcite that is coeval with the formation of diopside, scapolite, and magnetite (Fig. 1). Although the paragenesis of this sample is relatively unconstrained, the lack of sulfides may indicate that this sample belongs to the early pre-mineralisation skarn assemblage. Calcite from sample Mt Elliott 2 (ME 2) is coeval with the formation of andradite, pyrite, chalcopyrite, pyrrhotite, and magnetite (Fig. 1). The close relationship between calcite and chalcopyrite in this sample indicates that it is associated with the main Cu–Au-bearing skarn assemblage.

2.3 Flin Flon volcanic massive sulfide (VMS) deposit, Canada

The Flin Flon Greenstone Belt stretches across central Manitoba through to east central Saskatchewan and hosts several world-class Zn–Cu VMS deposits including the Flin Flon, Callinan, and 777 deposits (Koo and Mossman, 1975). Zn–Cu mineralisation is interpreted as having formed contemporaneously with deposition of the 1888.9 ± 1.6 Ma Millrock Member during the Trans-Hudson Orogeny (Koo and Mossman, 1975; Rayner, 2010; Gibson et al., 2012). The Flin Flon Zn–Cu orebody is recognised as having undergone six distinct deformation events that have affected the shape of the deposit (Lafrance et al., 2016; Schetselaar et al., 2017). “D₁” and D₂ were associated with the intra-oceanic

accretion of the Flin Flon Arc to other volcanic terrains before ca. 1872 Ma (Lafrance et al., 2016). D₃ occurred from 1847–1842 Ma as a response to the final accretion of the Flin Flon Terrane to the Glennie Terrane, producing west-verging folds within stacked, east-dipping thrust sheets of basement and cover rocks bounded by NNW-striking thrust faults (Lafrance et al., 2016). “D₄” resulted from the collision between the Flin Flon and Glennie Complex with the Sask Craton and is broadly coeval with the ca. 1840 Ma Phantom Lakes dyke (Gibson et al., 2012; Lafrance et al., 2016). “D₅” deformation produced a penetrative regional cleavage (S₅) that is defined by a continuous chloritic foliation ubiquitous in the volcanic basement rocks (Gibson et al., 2012; Lafrance et al., 2016). EWE–WNW-directed compression during “D₆” deformation produced a second regional penetrative cleavage and reactivated a variety of regional-scale faults (Gibson et al., 2012; Lafrance et al., 2016). Regional greenschist to granulite facies metamorphism is associated with D_{5–6} deformation at ca. 1820–1790 Ma (Schneider et al., 2007). The Flin Flon mine horizon was imbricated during D₃ thrusting with the shape of the ore lenses moulded during D₄ and D₅ deformation (Schetselaar et al., 2017). Regional greenschist to amphibolite grade metamorphism occurred between 1820–1790 Ma (U–Pb monazite; Schneider et al., 2007), with rocks in the Flin Flon deposit reaching greenschist facies (Koo and Mossman, 1975). The sample selected for this study is from the hydrothermally altered and sheared footwall of the Flin Flon VMS deposit. This sample is composed of highly foliated chlorite and calcite with disseminated pyrite and residual titanomagnetite. A band of highly foliated calcite was selected for Lu–Hf analysis (sample FF014; Fig. 1) to constrain the age of syn-metamorphic shearing of the deposit.

2.4 Yates U–Th prospect, Otter Lake area, Grenville Province, Canada

The Otter Lake area is located in SE Ontario within the Grenville Province. The Grenville Province can be distinguished from surrounding provinces based on various structural, metamorphic, and isotopic signatures attributed to the overprinting ca. 1080–980 Ma Grenvillian Orogeny (Rivers, 2015). This orogenic event produced widespread metamorphism from granulite to amphibolite facies (van Breemen and Corriveau, 2005) accompanied by widespread hydrothermal alteration in the Otter Lake area (Kretz et al., 1999). The Yates U–Th prospect is located approximately 100 km northwest of Ottawa and is renowned for the occurrence of pegmatites that contain large euhedral crystals of apatite set within a matrix of predominantly orange–pink calcite, with diopside, allanite, titanite, fluorite, thorite, and phlogopite (Schumann et al., 2019). A wide range of dates have been produced from the Yates mine, including titanite Pb–Pb and U–Pb ages between ca. 1020 and 998 Ma (Frei et al., 1997; Kennedy et al., 2011); apatite Pb–Pb and U–Pb

ages of 913 ± 7 Ma (Barfod et al., 2005), 933 ± 12 , and 920 – 850 Ma (Chew et al., 2011; Xiang et al., 2021); and an apatite Lu–Hf age of 1031 ± 6 Ma (Barfod et al., 2005). In addition, Simpson et al. (2021a) obtained an in situ Lu–Hf apatite age of 1000 ± 11 Ma (when corrected for laser-induced elemental fractionation). Importantly, the apatite Lu–Hf and Pb–Pb ages were obtained from the same large apatite crystal, indicating that the Lu–Hf and U–Pb systems were decoupled (as opposed to multiple generations of apatite growth). Barfod et al. (2005) argued that late-stage fluid interactions may have affected Pb retentivity in the apatite, as the apatite was unlikely to be above the apatite Pb closure temperature at ca. 913 Ma. Calcite from a specimen containing coarse-grained euhedral apatite with pink calcite, quartz, and diopside was selected for calcite Lu–Hf analysis (OL-MB, Fig. 1). The apatite is enclosed in the sampled calcite and is interpreted as having crystallised just prior to the calcite but during the same hydrothermal event.

3 Method

The samples were mounted in 2.5 cm diameter epoxy mounts and screened for Lu concentration by LA-ICP-MS to determine suitability for Lu–Hf analysis. Mineral liberation analysis (MLA) maps were obtained using a Hitachi SU3800 scanning electron microscope (SEM) to reveal the petrogenetic context of the analysed calcite.

3.1 In situ Lu–Hf dating method

Analysis was conducted at Adelaide Microscopy, the University of Adelaide. Calcite samples were analysed using a RESOLUTION 193 nm laser ablation system (Applied Spectra) with a S155 sample chamber (Laurin Technic). The laser ablation system was coupled to an Agilent 8900 tandem mass spectrometer (ICP-MS/MS). The methodology largely follows that of Simpson et al. (2021a) including an initial instrument tune conducted with no NH_3 in the reaction cell to achieve robust plasma conditions ($\text{U}/\text{Th} = 1.00$ – 1.05) and minimal oxide interferences ($\text{ThO}/\text{Th} < 0.2\%$). A carrier gas of 3.5 mL min^{-1} N_2 was added after the sample cell in order to increase sensitivity (Hu et al., 2008). Analytical conditions are included in Table D1.

Methods for the separation of ^{176}Hf from ^{176}Lu and ^{176}Yb follow that of Simpson et al. (2021a). In more detail, the Agilent 8900x utilises a reaction cell between two quadrupole mass analysers, which can be used to separate isobaric interferences. The first quadrupole is used as a mass filter (e.g. when set to mass 176, only ^{176}Lu , ^{176}Yb , and ^{176}Hf can pass), thereby minimising potential background interferences and other, unwanted reactions. Following this, a mixture of 10% NH_3 and 90% He is added to the reaction cell (at a rate of 3 mL min^{-1}). This mixture is optimised to promote formation of the Hf reaction product $\text{Hf}(\text{NH})(\text{NH}_2)(\text{NH}_3)_3^+$, and the second quadrupole is

set to 82 amu higher than the first (e.g. $\text{Q1} = 176$ amu and $\text{Q2} = 258$ amu). This method minimises the equivalent Lu and Yb reaction products ($\sim 0.03\%$ for Lu and below detection for Yb), such that the isobaric interferences on ^{176}Hf are negligible (Simpson et al., 2021a). Lens voltages were tuned to increase sensitivity on the Hf reaction product (Simpson et al., 2021a). In order to calculate Lu/Hf ratios, ^{176}Hf (+82) was measured directly, ^{175}Lu was measured as a proxy for ^{176}Lu , and ^{178}Hf (+82) was measured as a proxy for ^{177}Hf (Simpson et al., 2021a). $^{176}\text{Hf}/^{176}\text{Lu}$, $^{176}\text{Lu}/^{177}\text{Hf}$, and $^{176}\text{Hf}/^{177}\text{Hf}$ ratios were calculated as part of the normalisation to NIST610, as opposed to separately converting measured ^{175}Lu and ^{178}Hf into ^{176}Lu and ^{178}Hf . In more detail, if we assume that the $^{176}\text{Lu}/^{175}\text{Lu}$ ratio (or $^{177}\text{Hf}/^{178}\text{Hf}$ ratio) is identical between NIST SRM 610 and all analysed samples, a correction factor calculated from the percentage difference between the $^{175}\text{Lu}/^{178}\text{Hf}$ ratio measured in NIST SRM 610 and the published $^{176}\text{Lu}/^{177}\text{Hf}$ will correct the unknowns for matrix-independent fractionation and differences in isotopic abundance. ^{43}Ca was measured for internal normalisation of trace element abundances, and the following isotopes were measured to monitor for inclusions: ^{27}Al , ^{47}Ti , ^{89}Y , ^{90}Zr , ^{140}Ce , and ^{172}Yb .

Lutetium abundances in most calcite samples are low (< 6 ppm), so we employed a large laser diameter of $257 \mu\text{m}$ and a repetition rate of 10 Hz to maximise sensitivity. High sensitivity is important in order to either measure common Hf (in this case ^{178}Hf) or demonstrate that ^{176}Hf is sufficiently above detection limits that the effects of common Hf are negligible. Smaller spot sizes could be employed for higher-Lu and/or higher-Hf samples. An extra 20 s delay was added after each interval of sample ablation in order to ensure the washout had reached background levels. NIST SRM 610 glass ($^{176}\text{Lu}/^{177}\text{Hf}$: 0.1379 ± 0.005 ; $^{176}\text{Hf}/^{177}\text{Hf}$: 0.282122 ± 0.000009 ; Nebel et al., 2009) was used as the primary reference material and was analysed using a spot size of $43 \mu\text{m}$. The smaller spot size was required to ensure that ^{175}Lu was measured in pulse counting mode (< 4 Mcps). Consistent with observations in Simpson et al. (2021a), Lu and Hf showed no measurable downhole fractionation in the analysed carbonates (Fig. 2); as such, no downhole correction was applied to the data.

A side effect of the use of large ablation spots is “plasma loading”, for which the introduction of a large amount of material reduces the ionising efficiency of the plasma (Kroslakova and Günther, 2007). Plasma loading was observed in the time-resolved signals, with a reduction in signal intensity for all isotopes after ~ 10 to 15 s of ablation. Following this, the signal stabilised after ~ 18 s of ablation (Fig. 2). Importantly, this variation in signal intensity was not observed in the calculated time-resolved isotope ratios (Fig. 2), which means that identical ratios were calculated whether this decrease in signal intensity was included in the ratio calculation or not. Importantly, plasma loading can be affected by sample matrix (Kroslakova and Günther, 2007),

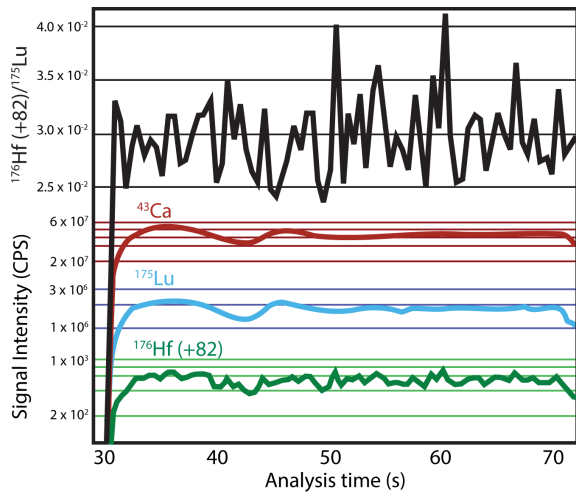


Figure 2. Time-resolved signals for $^{175}\text{Lu} / (^{176})\text{Hf} (+82)$, ^{43}Ca , ^{175}Lu , and $(^{176})\text{Hf} (+82)$ demonstrating the effects of plasma loading on the signal intensities (i.e. dip in signal intensities at ~ 10 – 15 s ablation) but not for the $^{176}\text{Hf} / ^{175}\text{Lu}$ ratio, which remains constant downhole. The time-resolved intensity of each analyte has been offset in the graph for better comparison; therefore the y axis scale is not continuous. Green horizontal lines show the scale for $^{176}\text{Hf} (+82)$, blue horizontal lines show the scale for ^{175}Lu , red horizontal lines show the scale for ^{43}Ca , and black horizontal lines show the scale for the $^{176}\text{Hf} (+82) / ^{175}\text{Lu}$ ratio. Presented data are from an analysis of MKED calcite.

especially for minerals containing easily ionised elements such as Ca. This necessitates matrix-matched calibration, despite the observed lack of downhole changes in Lu–Hf ratios (Simpson et al., 2021a).

The large ablation volume caused accumulation of ablated material in the tubing and on the interface cones during the first analytical session, which coincided with a decrease in signal intensity over time. Consequently, session 1 records slightly more signal drift compared to session 2. However, there was no measurable corresponding drift observed in the calculated isotopic ratios, apart from a slight decrease in precision due to the lower sensitivity toward the end of the run. Therefore, we recommend that cones are cleaned prior to analysis, and suggest a maximum session duration of approximately 7 h when using spot diameters of $> 200 \mu\text{m}$. In addition to this, the accumulated material was sometimes mobilised in later analyses, potentially contaminating data. This was observed by increases in Al during the start of ablation that decayed down to background levels. Importantly, similar Al spikes were not observed during background measurement, indicating that contamination due to material remobilised during ablation is likely; hence the additional 20 s of washout did not fix this. This contamination did not generally produce a measurable effect on calculated Lu / Hf ratios. However, we stress that this contamination is important to monitor as Hf concentrations are sometimes in the parts

per trillion level. As such we recommend close monitoring of signals, particularly Al concentrations, and the removal of 1–3 s of each analysis after signal stabilisation if necessary.

3.2 Data processing

For both LA-ICP-MS and LA-ICP-MS/MS analysis, a stoichiometric Ca concentration of 40.04 wt % for calcite was used for internal normalisation of trace element concentrations. Although the high Ca counts per second for all analysed samples indicate that they are close to stoichiometric calcite, there may be slight inaccuracies in calculated element concentrations due to major element substitutions from Mg, Fe, and Mn that are common in carbonates. However, element concentrations were largely used as relative proxies to monitor for inclusions.

Background subtractions, element concentrations, and ratio calculations were performed using the LADR software (Norris and Danyushevsky, 2018). Where ^{178}Hf was measured above detection limits (~ 2 ppt for ^{178}Hf), common-Hf corrections were applied to the data after background subtractions but prior to normalisation to the standard. In more detail, the ^{178}Hf counts per second measurement for each sampling cycle of the analysis period of each laser spot was used to calculate the common-Hf component of the corresponding ^{176}Hf cycles per second measurement, using the following equation:

$$^{176}\text{Hf}_r = ^{176}\text{Hf}_m - \left(\left(\frac{^{176}\text{Hf}}{^{178}\text{Hf}} \right)_c \times ^{178}\text{Hf}_m \right), \quad (1)$$

where $^{176}\text{Hf}_r$ is radiogenic ^{176}Hf , $^{176}\text{Hf}_m$ is measured ^{176}Hf , $^{178}\text{Hf}_m$ is the measured ^{178}Hf , and $\left(\frac{^{176}\text{Hf}}{^{178}\text{Hf}} \right)_c$ is the initial or common- $^{176}\text{Hf} / ^{178}\text{Hf}$ ratio. These corrections were applied using an assumed initial $^{176}\text{Hf} / ^{178}\text{Hf}$ ratio of 0.192 ± 0.004 , which is equivalent to a $^{176}\text{Hf} / ^{177}\text{Hf}$ ratio of 0.2816 ± 0.006 . This value is based on the Hf evolution of the crust, with an uncertainty that comfortably covers likely natural variation. The uncertainty in the initial $^{176}\text{Hf} / ^{178}\text{Hf}$ ratio used for the common-Hf corrections has been propagated to the final ages, in order to account for any inaccuracies introduced by the value used. However, as most analyses have $< 1\%$ common Hf (Table 1), any inaccuracy related to the initial $^{176}\text{Hf} / ^{178}\text{Hf}$ ratio is negligible compared to the total uncertainty estimates, given Hf isotopes do not vary significantly with time (Vervoort, 2014; Fisher and Vervoort, 2018). Such corrections, however, should be used with caution for samples with higher common Hf, although the dataset presented in this study is not sufficient to determine what an appropriate cutoff should be.

Subsequent to this correction, isotopic ratios were corrected using an external reference material bracketing approach (commonly used in LA-ICP-MS geochronology), with primary and secondary reference materials interspaced with unknowns through each analytical session. The data

Table 1. Ages and Lu and Hf concentration information for the analysed samples.

Sample	Age (Ma)	95 % CI	<i>n</i>	Min % Hf corr	Avg % Hf corr	Max % Hf corr	Min Lu ppm	Avg Lu ppb	Max Lu ppb	Min Hf* ppb	Avg Hf* ppb	Max Hf ppb
P01	2054	1.5 %	36	0 %	2.65 %	13 %	270	505	557	0.03	0.270	1.00
LC 1	1513	1.7 %	19	0.16 %	0.46 %	1.25 %	1900	1600	3600	0.011	0.090	0.360
ME 1	1540	0.6 %	79	0 %	0.28 %	2.4 %	4300	5325	6300	0.002	0.150	1.80
ME 2	1500	0.9 %	29	0.16 %	0.58 %	3.04 %	700	3159	5500	0.002	0.110	0.340
OL-MB	892	1.2 %	30	0.16 %	0.58 %	1.25 %	1100	1200	1300	0.003	0.050	0.120
FF014	1807	1.0 %	35	0.16 %	0.39 %	1.3 %	616	1020	1170	0.004	0.052	0.210

Note: 95 % CI refers to the 95 % confidence interval uncertainty in the calculated age. *n* refers to the number of analyses used for the age calculation. % Hf corr refers to the average percentage decrease in age due to the common-Hf correction. Hf* concentrations have been calculated from ^{178}Hf and assume no radiogenic ingrowth of ^{176}Hf and thus represent the “common” Hf concentration for each sample.

were normalised to NIST SRM 610 glass to correct for drift and matrix-independent fractionation. The Lu–Hf isotopic ratios published in Nebel et al. (2009) were used for the NIST610 SRM normalisation. Following this, $^{176}\text{Hf}/^{176}\text{Lu}$, $^{176}\text{Lu}/^{177}\text{Hf}$, and $^{176}\text{Lu}/^{176}\text{Hf}$ ratios were corrected to MKED calcite. Although the age of MKED calcite is currently not independently constrained, calcite is interpreted from textural evidence to have formed with the MKED titanite reference material, and therefore the titanite thermal ionising mass spectrometry (TIMS) U–Pb age was used (1517.32 ± 0.32 Ma; Spandler et al., 2016). Further details are outlined in Appendix A. This correction method is similar to that used by Roberts et al. (2017) for calcite U–Pb, where the observed analytical offset between the measured and expected Lu–Hf ratio in the standard is applied (as a percentage correction factor) to the ratios of the unknowns. This offset is inferred to be due to a combination of laser-induced (matrix-dependent) elemental fractionation and plasma loading. The uncorrected ages for MKED calcite as well as for ME 1 across four analytical sessions are constant within uncertainty, indicating that the age offset is a systematic analytical bias that is applicable to the calcite samples of unknown age (Fig. A2). Weighted average ages were calculated using ISOPLOT (Vermeesch, 2018), using the ^{176}Lu decay constant determined by Söderlund et al. (2004): $0.00001867 \pm 0.00000008 \text{ Myr}^{-1}$.

Correct handling of uncertainties in geochronology is important in order to draw accurate conclusions about the resulting ages. As per the recommendations for LA-ICP-MS U–Pb uncertainty propagation in Horstwood et al. (2016), uncertainties are categorised as random, in which case they are propagated to individual analyses, or systematic, in which case they are propagated to the final calculated age. As such, the uncertainties associated with the measurement of the primary standard (NIST SRM 610) have been propagated to the uncertainties of individual analyses. The following systematic uncertainties have been propagated to the final ages: measurement uncertainty in the secondary standard (MKED C), uncertainty in the titanite U–Pb age used as the reference age for MKED C, uncertainties associated with

the ^{176}Lu decay constant, and the reference $^{176}\text{Hf}/^{177}\text{Hf}$ ratios for NIST SRM 610. Although for completeness it would be good to propagate uncertainty relating to potential differences in $^{175}\text{Lu}/^{176}\text{Lu}$ and $^{177}\text{Hf}/^{178}\text{Hf}$ between NIST SRM 610 and samples (i.e. natural variation in these ratios), currently there appear to be no data on this. These uncertainties are likely to be negligibly small relative to the overall uncertainty estimates for the analyses. The uncertainty associated with the reference $^{176}\text{Lu}/^{177}\text{Hf}$, $^{176}\text{Lu}/^{176}\text{Hf}$, and $^{176}\text{Hf}/^{176}\text{Lu}$ ratios of NIST SRM 610 is not propagated, as the correction factor associated with NIST610 SRM is cancelled during the correction to MKED calcite (as the NIST610 SRM correction factor is applied equally to MKED calcite and the unknowns samples and thus becomes redundant). Uncertainty relating to long-term reproducibility of the standards has not been propagated, as the standard data for all sessions do not show scatter outside of what would be expected from a single population. More data, however, are required to fully constrain this.

4 Lu–Hf results

The analysed calcite generally contains < 1 % common Hf, apart from sample P01, which contains up to 13 % common Hf in individual analyses (Table 1). Consequently, the common-Hf corrections are small (or effectively non-existent), and the resultant ages are not significantly affected by the assumed initial $^{176}\text{Hf}/^{177}\text{Hf}$ ratio. Corrected and uncorrected data are included in the supplementary data set by Simpson (2021). The inverse isochron and weighted mean single-spot Lu–Hf ages, reported below, are corrected against MKED calcite for matrix-dependent fractionation and are common-Hf corrected (where relevant) (Fig. 3). For analyses with inclusions, the signals have been cropped to remove inclusions or, in the case of more significant signal disturbances, excluded from age calculations. Inclusions were detected in the following samples: MKED calcite (6), LC1 (1), P01 (19), and FF014 (6). Excluded data points are included in Simpson (2021). Due to the large number of inclusions, P01 was analysed over two sessions. Data are presented as

inverse isochrons (Li and Vermeesch, 2021) and as common-Hf-corrected weighted average ages (Fig. 3).

5 Discussion

The Phalaborwa carbonatite sample produced a Hf-corrected weighted average Lu–Hf age of 2050 ± 30 Ma (Fig. 3), consistent with previous baddeleyite U–Pb SIMS ages (~ 2060 Ma; Wu et al., 2011). Importantly, the consistency between the calcite Lu–Hf age and existing constraints on carbonatite formation demonstrates that calcite Lu–Hf dating can produce primary age information for early Paleoproterozoic calcite. This result also demonstrates that calcite Lu–Hf geochronology is a viable technique to directly date carbonatite magmatism and associated mineralisation, even in the case of old calcite samples with only ~ 0.5 ppm Lu.

The weighted average Lu–Hf ages for samples ME 1 and ME 2 are 1538 ± 9 and 1504 ± 13 Ma respectively (Fig. 3). The ages of these samples are consistent with the paragenetic timing of alteration at Mt Elliott, providing evidence for calcite precipitation during at least two temporally distinct alteration events. Sample ME 1 is from a coarse calcite–diopside–scapolite–magnetite vein that does not contain sulfides (Fig. 1); the age is, therefore, consistent with formation prior to the major ~ 1510 Ma Cu–Au mineralisation event (Duncan et al., 2011; Wang and Williams, 2001). In addition, this age overlaps with a titanite U–Pb age from the Mt Elliott deposit (1530 ± 11 Ma; Duncan et al., 2011) and is potentially related to regional Na–Ca alteration between ca. 1555 and ca. 1521 Ma (Oliver et al., 2004). The 1504 ± 13 Ma age obtained from sample ME 2 that has an ore-stage paragenesis conforms with the $^{207}\text{Pb}/^{206}\text{Pb}$ age of cogenetic andradite (1507 ± 35 Ma; Appendix B) and overlaps with the ca. 1510 Ma main mineralisation event (Wang and Williams, 2001; Duncan et al., 2011). Additionally, data for ME1 were pooled from all four analytical sessions in order to test reproducibility. Similar to the standard (MKED1; Appendix A), ME1 does not show excess scatter between sessions (Fig. 3).

Sample LC1, from the Lime Creek quarry, Eastern Fold Belt, Mt Isa Inlier produced an age of 1513 ± 26 Ma, consistent with published titanite U–Pb ages (1521 ± 5 , 1527 ± 7 Ma) from the nearby Knobby Quarry (Oliver et al., 2004). Additionally, this age is consistent with the intrusion of the ca. 1530–1500 Ma Williams–Naraku batholiths, which are interpreted as being the source of the fluids from which the calcite precipitated (Page and Sun, 1998; Oliver et al., 1993). Our results for this sample further demonstrate that calcite Lu–Hf geochronology is an effective technique for constraining the age of calcite mineralisation.

Sample OL-MB from Otter Lake produced a Lu–Hf age of 892 ± 12 Ma (Fig. 3). This age is significantly younger than the apatite solution Lu–Hf age of 1030 ± 6 Ma (Barfod et al., 2005) and the in situ apatite Lu–Hf age of 1000 ± 11 Ma (Simpson et al., 2021a) but is similar to the apatite Pb–Pb

age of 913 ± 7 Ma (Barfod et al., 2005) and the latest stage of extensional activity on the nearby Bancroft Shear Zone (1045–893 Ma, Ar–Ar phlogopite; Cosca et al., 1995). Given the similarity between the ca. 0.9 Ga ages, obtained by different methods, it seems likely that the calcite either grew or records Lu–Hf isotopic resetting during the same event that induced resetting of the apatite Pb–Pb system. The slight difference between the calcite Lu–Hf age (894 ± 12 Ma) and apatite Pb–Pb age (913 ± 7 Ma) may be due to analytical (i.e. mixing of age domains in the solution Pb–Pb age) rather than geological reasons, particularly given an individual crystal of apatite from the Yates mine produced a U–Pb age range of 920–850 Ma (Xiang et al., 2021). The age difference may also be due to the underestimation of uncertainties. Large (~ 3 cm) apatite crystals such as the one analysed by Barfod et al. (2005) are expected to have Pb closure temperatures of up to 600°C (Krogstad and Walker, 1994; Barfod et al., 2005), giving a possible upper limit to Lu–Hf closure in calcite. We note that this is significantly higher than the closure temperature of Ar–Ar in phlogopite (ca. 400°C), indicating that the Otter Lake area potentially had a different thermal history and/or that isotopic resetting in the apatite and calcite was aided by late fluid interactions, as hypothesised by Barfod et al. (2005). As such, further work is required to constrain the Lu–Hf closure temperature in calcite.

The in situ Lu–Hf age of 1810 ± 18 Ma for the cleavage-hosted calcite vein from the Flin Flon VMS deposit (FF14; Fig. 3), as expected, is younger than the timing of initial mineralisation at the deposit (Rayner, 2010; Koo and Mossman, 1975; Stern et al., 1995). Instead, the age is in excellent agreement with ca. 1820–1790 Ma regional peak greenschist to amphibolite grade metamorphism (Schneider et al., 2007), suggesting the calcite precipitated during metamorphism related to deformation stage D₅ or D₆, associated with the final collision between the Flin Flon–Glennie Complex and the Sask Craton (Lafrance et al., 2016). This regional event locally reached maximum greenschist-facies metamorphism (Koo and Mossman, 1975), suggesting the calcite grew under low-grade metamorphic conditions. Sample FF014, therefore, demonstrates that calcite Lu–Hf geochronology has the potential to date low-grade metamorphism, which has been difficult using traditional dating methods (e.g. Henrichs et al., 2018).

In summary, we demonstrate that in situ Lu–Hf geochronology can produce geologically meaningful ages for calcite from a variety of mineralisation styles (e.g. IOCG, carbonatite, and skarn alteration) as well as greenschist-facies metamorphism. The technique also has great potential to date a range of other geological settings and processes (e.g. chemical sedimentation, carbonation reactions) provided calcite contains sufficient Lu for analysis.

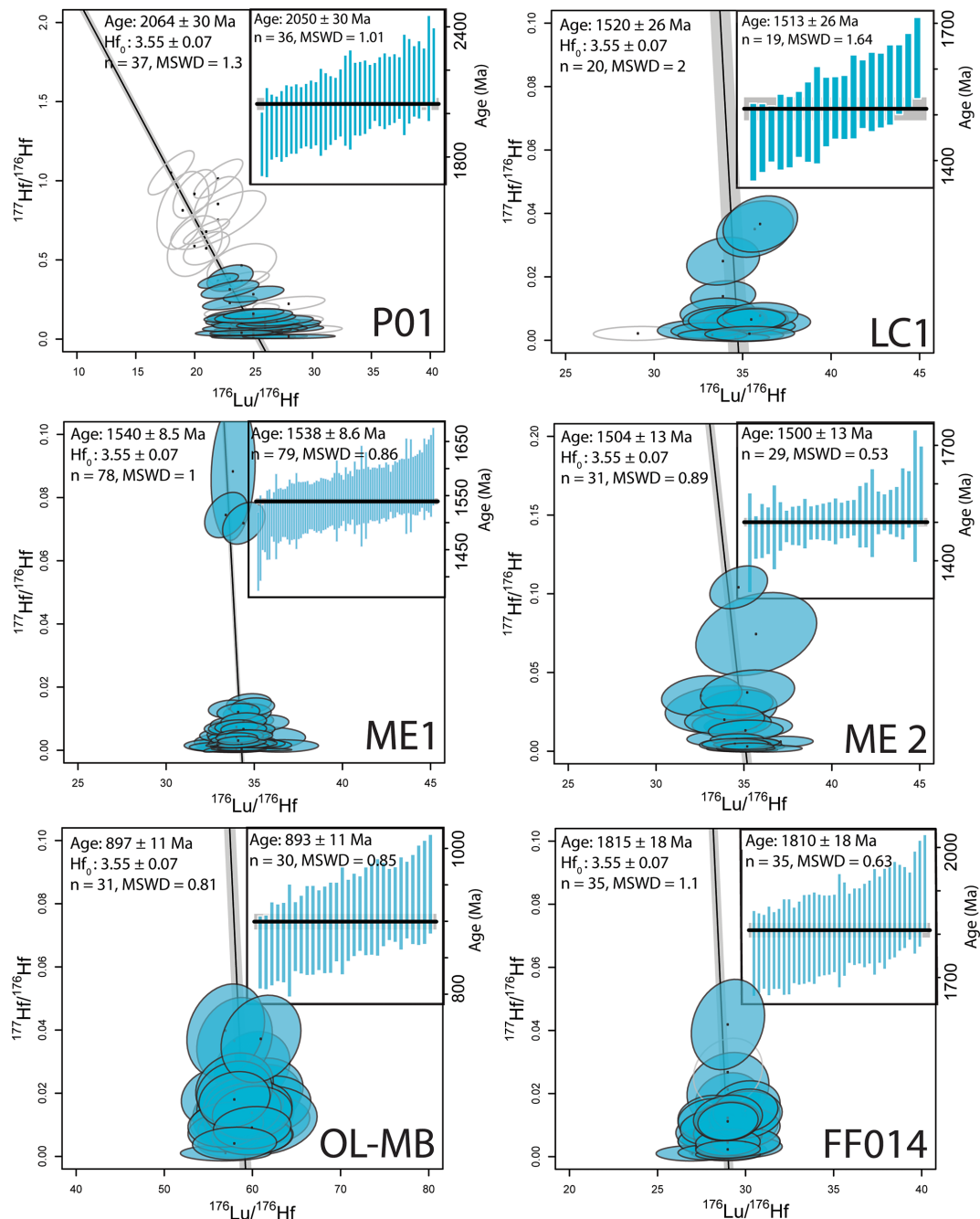


Figure 3. Anchored inverse isochron and weighted average “single-spot” ages for analysed samples, corrected for matrix-induced fractionation against MKED1 calcite. Isochrons have been anchored to an initial $^{177}\text{Hf}/^{176}\text{Hf}$ ratio of 3.55 ± 0.07 . Ellipses represent data points and 2σ uncertainty. Weighted average ages are corrected for common-Hf where relevant (see Table 1 and text). Blue bars represent 2σ uncertainties. Black lines represent weighted average ages, with grey boxes representing the 95 % confidence interval uncertainty.

5.1 Limitations

The success rate of the in situ Lu–Hf dating approach in calcite is intrinsically related to (1) the concentration of Lu and (2) the ingrowth time for radiogenic Hf (Fig. 4). Generally, the method is more suitable for REE-rich calcite typically observed in mineral deposits and carbonatites, and/or for Pre-

cambrian samples. In addition, the currently available mass spectrometers require large laser beam diameters ($257\ \mu\text{m}$) for successful calcite Lu–Hf dating, limiting spatial resolution compared to most laser ablation dating techniques. We note that for high-Lu samples, such as ME 1 (or samples that incorporate common Hf), smaller spot sizes are feasible. Ad-

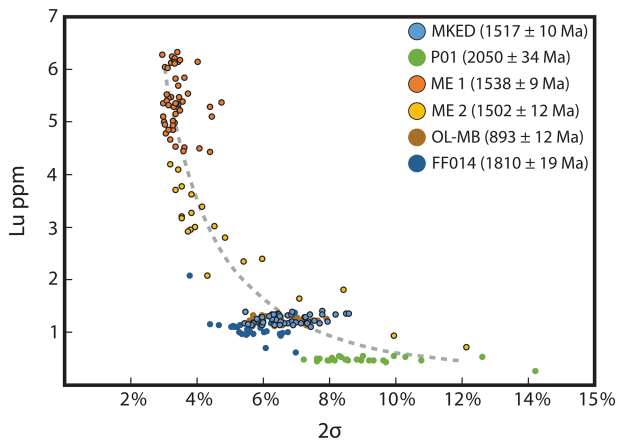


Figure 4. Lu parts per million vs. 2σ uncertainty for each calcite analysis. The grey curve shows a function fitted to the data from samples with ages between 1500 and 1540 Ma (samples ME 1, ME 2, and MKED, with symbols outlined in black). Only data points with similar ages were used to construct this guiding curve as the obtained precision is age-dependent. The Lu–Hf ages for older samples (e.g. P01 and FF014) are more precise relative to younger samples for a given Lu concentration (assuming no common Hf). Note: MKED is the calcite Lu–Hf standard used to correct the analysed samples. All data for MKED are included in Simpson (2021).

ditionally, particularly in hydrothermal settings, calcite often forms large, millimetre- to centimetre-scale crystals, reducing the need for small ablation volumes. While individual calcite crystals in other settings can sometimes be $< 260 \mu\text{m}$, the total amount of calcite is often large enough that aggregates of pure (or close to pure) calcite can be ablated. Caution should be used with such analysis, however, as this may affect laser-induced fractionation, individual crystals may be of different ages, and there may be micro-inclusions of other minerals.

5.2 Advantages of in situ Lu–Hf dating of calcite compared to other geochronological methods

The previous dissolution-based Lu–Hf geochronology has produced scattered isochrons, indicative of isotopic disturbances (Maas et al., 2020). While individual data points are significantly less precise than dissolution-based methods, the ability to gain spatially resolved data on a much smaller scale ($> 260 \mu\text{m}$) as well as to obtain a large number of analyses in a single session can make data interpretation easier (Simpson et al., 2021a). Importantly, trace element data can be obtained simultaneously to interrogate each data point for inclusions or age zonation. Furthermore, calcite Lu–Hf dating can overcome two issues often encountered during U–Pb dating: (1) in contrast to Pb, calcite does not incorporate significant concentrations of common Hf, and (2) Lu is comparatively resistant to thermal diffusion in calcite (Cherniak, 1997), increasing the likelihood of primary precipitation ages being

preserved. However, it should be acknowledged that fluid mobility and recrystallisation of the calcite may affect Lu–Hf ages and are difficult to predict. This opens the possibility that time constraints can be obtained for carbonates from the first three-quarters of Earth history that are generally difficult to date by other methods. Importantly, calcite is commonly associated with ore formation, meaning in situ Lu–Hf dating affords the possibility to directly constrain the age of mineralising events and the temporal evolution of mineral deposit systems.

From our work, we suggest samples ME1 and OL-MB calcite could be developed as primary reference materials due to being (1) common-Hf free, (2) homogenous in age across crystals up $\sim 1 \text{ cm}$ in size, and (3) available in large quantities. We aim to characterise such reference materials and make them available to the wider geochronology community.

6 Conclusions and future directions

Calcite is among the most common of rock-forming minerals, meaning that in situ Lu–Hf geochronology of calcite has enormous potential to constrain the age of formation and/or alteration of a range of igneous, sedimentary, metamorphic, and hydrothermal rock systems, including rock types that are considered very difficult to date (e.g. marbles). This technique has particular application to mineral deposits as it allows for the ability to constrain the age of pre-ore, ore-stage, and post-ore events (e.g. Fig. 3). Furthermore, given the successful dating of old ($\sim 2 \text{ Ga}$) calcite with $< 1 \text{ ppm}$ Lu (e.g. sample P01; Table 1), this technique has the potential to date old calcite from a variety of settings with relatively low heavy rare earth element (HREE) concentrations. In situ Lu–Hf dating of calcite can be regarded as a complementary, and in some cases alternative, technique to carbonate U–Pb dating, where Lu–Hf dating is well suited for older samples, or to obtain primary precipitation ages for systems affected by Pb mobility. Coupling in situ Lu–Hf dating with other isotopic systems (U–Th–Pb, C, O, Sr, Nd) may be particularly powerful for constraining the origin, nature, and redox conditions of the fluids or melts from which the calcite precipitated.

Appendix A: MKED calcite sample description

A sample of orange–pink calcite associated with the MKED1 titanite U–Pb standard ($1517.3 \pm 0.3 \text{ Ma}$, U–Pb TIMS; Spandler et al., 2016) was analysed as a matrix-matched secondary standard in order to correct unknown samples for matrix-related analytical offsets, such as laser-induced elemental fractionation and plasma loading effects. The calcite was sampled from the same drill core from which the titanite standard was taken (full details can be found in Spandler et al., 2016). The sample consists of massive calcite surrounding large ($\sim 8 \text{ cm}$) euhedral titanite crystals. The titanite is interpreted as having grown in the same fluid as the calcite but

just prior to calcite crystallisation. The average age across all four analytical sessions is 1560 ± 10 Ma (Fig. A1), suggesting that matrix fractionation during laser ablation produces ages that are systematically approximately 3 % too old.

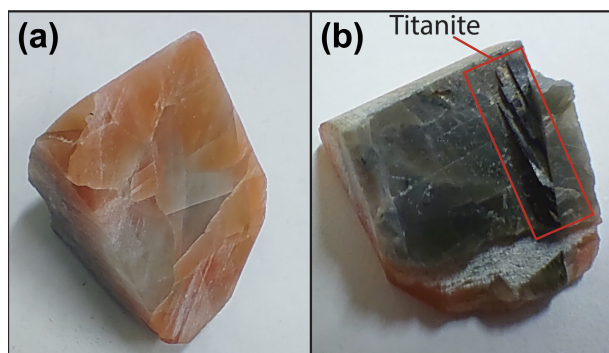


Figure A1. Images of MKED calcite. Panel (a) shows calcite chip from where the analysed sample was taken. Panel (b) shows underside of the same chip, where a large titanite crystal has been removed. Red box shows remnant fragments of titanite.

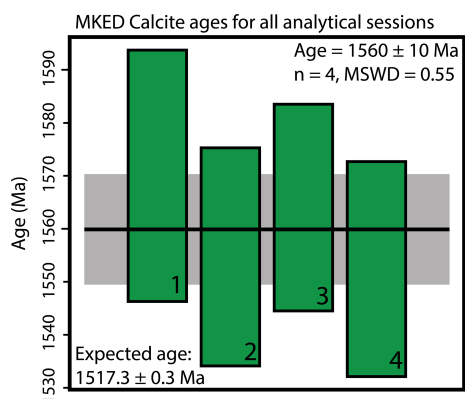


Figure A2. Demonstration of the systematic analytical offset observed for calcite Lu–Hf ages. Green rectangles are 95 % confidence intervals around weighted mean ages for each session, with the session number in the bottom right corner of each rectangle. Horizontal black line shows the weighted average age of all analytical sessions, with the grey rectangle showing 95 % confidence interval uncertainty. The combined weighted average age for all analytical sessions is shown in the top right corner. The expected age is from Spandler et al. (2016). Weighted mean ages were calculated using ISOPLOT (Vermeesch, 2018).

Appendix B: Mt Elliott andradite U–Pb data

Cogenetic andradite was analysed from the Mt Elliott 2 calcite sample (Fig. 1). The sample was analysed using the same laser system as used for Lu–Hf analysis but coupled with an Agilent 7900 quadrupole mass spectrometer. As the University of Adelaide does not currently possess an andradite U–Pb standard, U–Pb and Pb–Pb ratios were corrected to NIST610 SRM, using ratios from Stern and Amelin (2003). A large aspect ratio ablation spot (120 μ m in diameter, drilling approximately 30 μ m deep) was used to minimise the effects of downhole fractionation (Sylvester, 2008); however, it is possible that calculated U–Pb ages are inaccurate due to the lack of matrix-matched primary standard. As the data appear to be concordant, however, a weighted average age can be calculated from the $^{207}\text{Pb}/^{206}\text{Pb}$ ratios (Fig. B1), which should not be significantly affected by laser-induced matrix fractionation. As such, the calculated age is considered accurate within uncertainty.

Appendix C: Large sample images

The following are larger versions of the sample images from Fig. 1. Mineral abbreviations are as follows: Cal – calcite; Cpy – chalcopyrite; Py – pyrite; Mag – magnetite; Cu – cubanite; Di – diopside; Scp – scapolite; An – andradite.

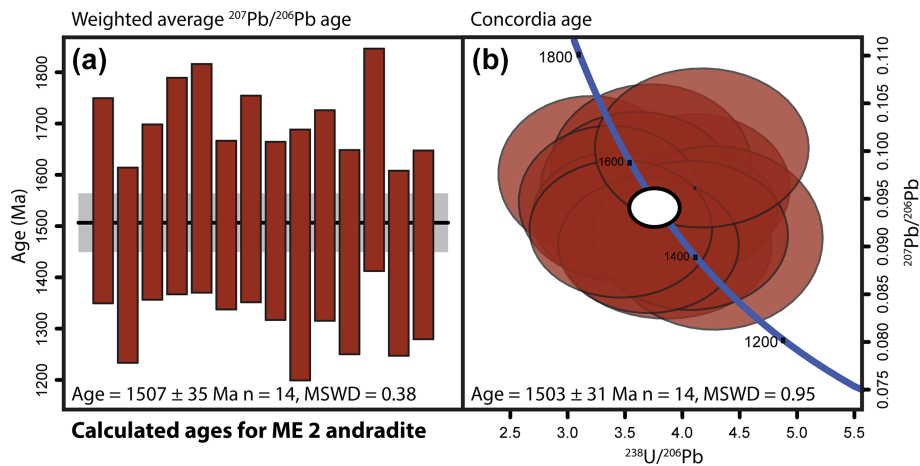


Figure B1. U–Pb age of ME 2 andradite. Panel (a) shows the weighted average $^{207}\text{Pb}/^{206}\text{Pb}$ age, and panel (b) shows the concordia age on a Tera–Wasserburg concordia plot. For the weighted average, vertical rectangles are 2σ uncertainties around calculated single-spot ages, with the black bar showing calculated weighted mean age and the grey rectangle showing associated 95 % confidence interval uncertainty. For the concordia plot, each ellipse shows the 2σ uncertainty around each analysis, with the white ellipse representing 95 % confidence interval uncertainty around the calculated concordia age. Weighted mean age and concordia age were calculated using ISOPLOT (Vermeesch, 2018).

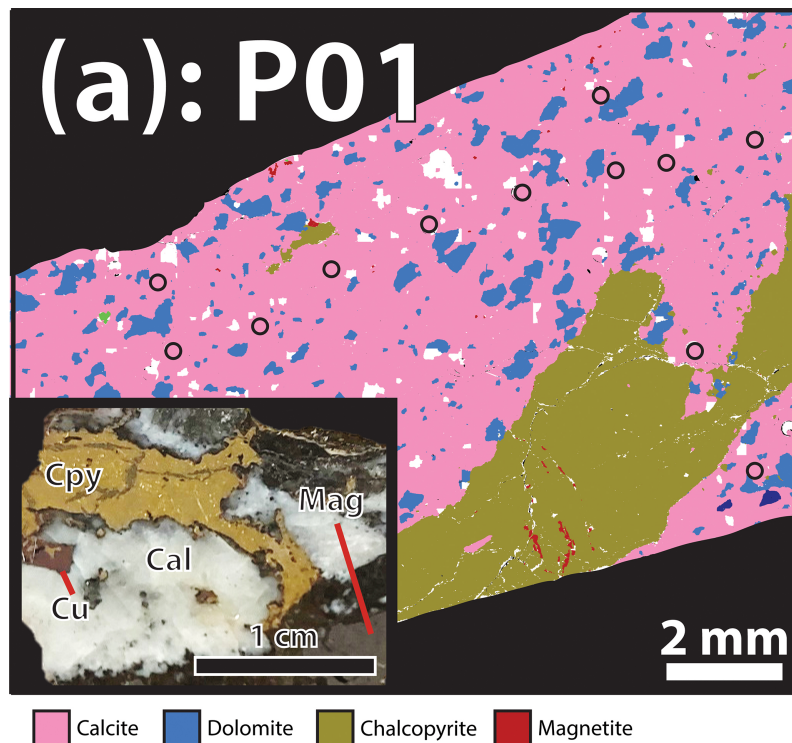


Figure C1. Large image of sample P01 from Phalaborwa carbonatite, South Africa. Large image shows SEM mineral map. Inset shows hand sample photo. Cpy: chalcopyrite; Cu: cubanite; Cal: calcite; Mag: magnetite.

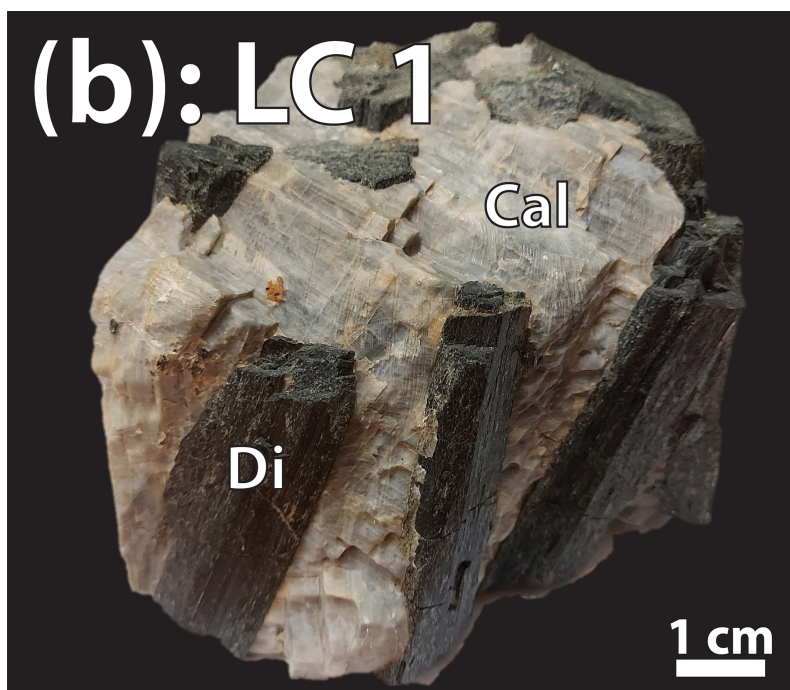


Figure C2. Large image of sample LC1 from Lime Creek, Mt Isa region, Australia. Image shows hand sample. Di: diopside; Cal: calcite.

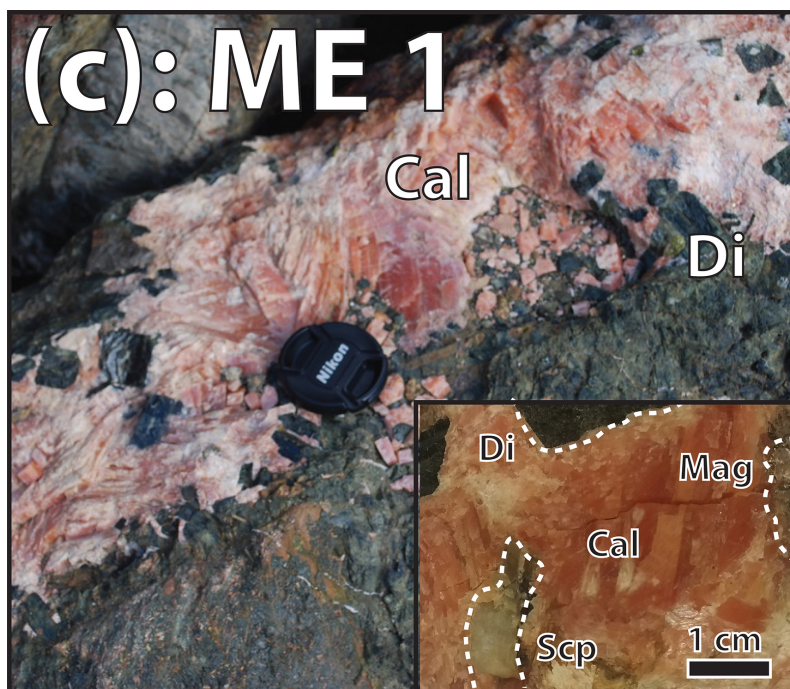


Figure C3. Large image of sample ME1 from Mt Elliott, Mt Isa region, Australia. Large images shows sample location and inset shows hand sample. Di: diopside; Scp: scapolite; Cal: calcite; Mag: magnetite.

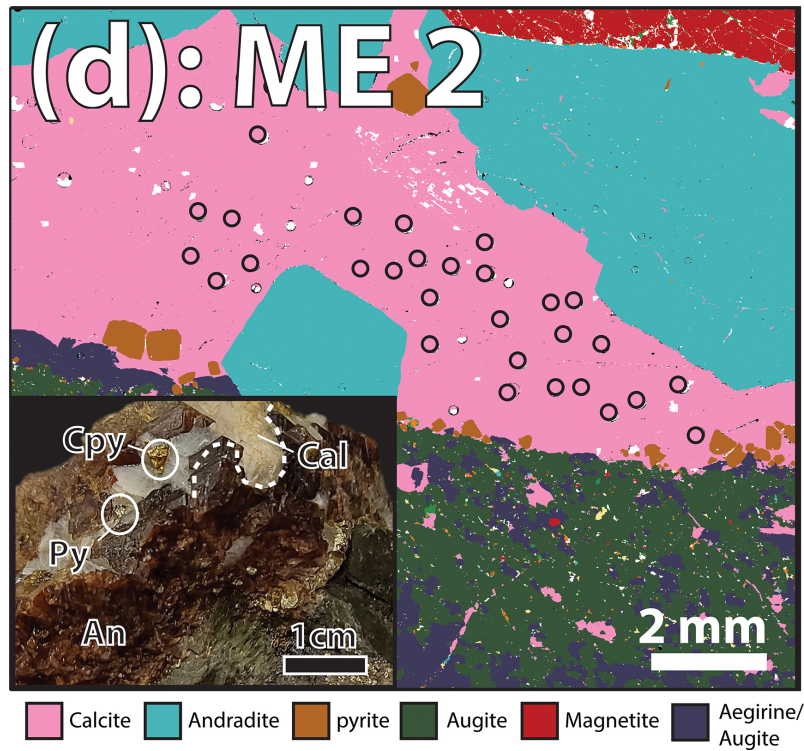


Figure C4. Large image of sample ME 2 from Mt Elliott, Mt Isa region, Australia. Large images shows SEM mineral map with black circles showing laser spot locations. Inset shows hand sample photo. Cpy: chalcopryrite; Py: pyrite; Cal: calcite; An: andradite.

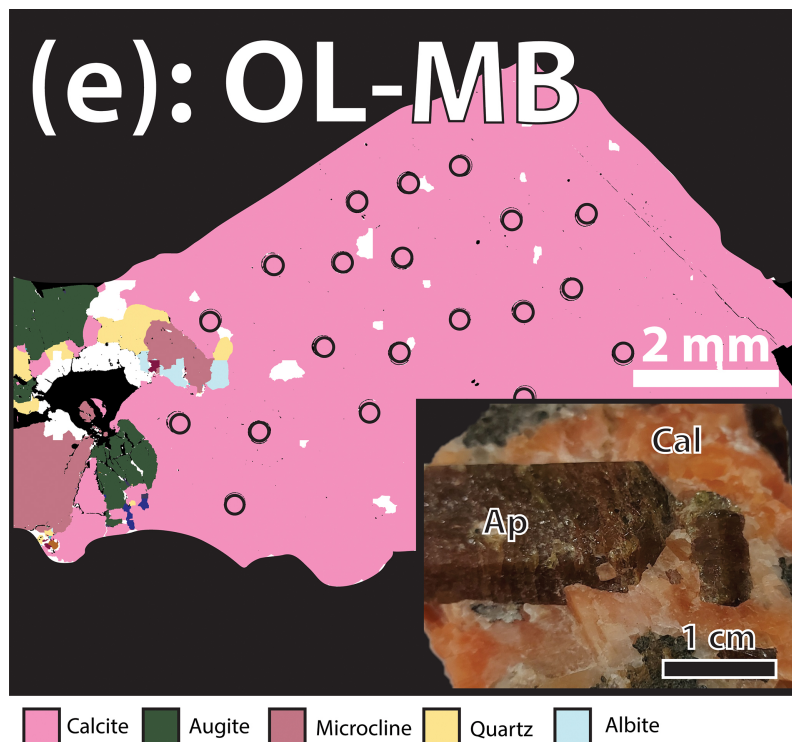


Figure C5. Large image of sample OL-MB from the Yates mine, Canada. Large images shows SEM mineral map with black circles showing laser spot locations. Inset shows hand sample photo. Ap: apatite; Cal: calcite.

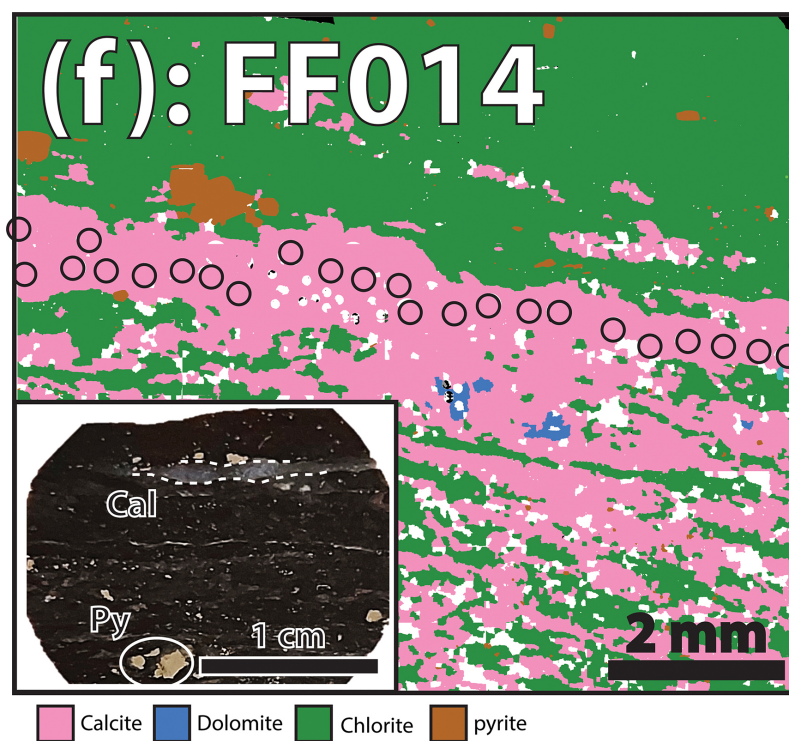


Figure C6. Large image of sample FF014 from Flin Flon, Manitoba and Saskatchewan, Canada. Large images shows SEM mineral map with black circles showing laser spot locations. Inset shows hand sample photo. Py: pyrite; Cal: calcite.

Appendix D

Table D1. Analysis and LA-ICP-MS/MS tuning parameters.

Plasma parameters	
Radio frequency (RF) power	1350 W
Sample depth	4 mm
Ar carrier gas	0.94 L min ⁻¹
He carrier gas	0.38 L min ⁻¹
N ₂ addition	3.5 mL min ⁻¹
Lens parameters	
Extract 1	–1.5 V
Extract 2	–140 V
Omega bias	–70 V
Omega lens	8.0 V
Q1 entrance	–45 V
Q1 exit	1.0 V
Cell focus	1.0 V
Cell entrance	–120 V
Cell exit	–100 V
Deflect	10.0 V
Plate bias	–60 V
Q1 parameters	
Q1 bias	–1.0 V
Q1 pre-filter bias	–10.0 V
Q1 post-filter bias	–10.0 V
Cell parameters	
He flow	1.0 mL min ⁻¹
10 % HN ₃ + 90 % He gas flow	3 mL min ⁻¹
Octopole bias	–2.0 V
Axial acceleration	2.0 V
Octopole RF	180 V
Energy discrimination	–13.0 V
Q2 parameters	
Q2 bias	–15 V
Wait time offset	5 ms
Analysis parameters	
Laser wavelength	193 nm
Laser fluence	10 J cm ⁻²
Laser spot diameter	257 μm (43 μm; NIST610 glass)
Laser repetition rate	10 Hz
Washout	30 s (post-cleaning pulse) + 20 s (post analysis)
Background	30 s
Analysis time	40 s
Isotopes measured/dwell times (ms)	²⁷ Al (2), ⁴³ Ca (2), ⁴⁷ Ti (2), ⁸⁹ Y (2), ⁹⁰ Zr (2), ¹⁴⁰ Ce (2), ¹⁷² Yb (10), ¹⁷⁵ Lu (10), ¹⁷⁵⁺⁸² Lu (100), ¹⁷⁶⁺⁸² Hf (150), ¹⁷⁸⁺⁸² Hf (150)

Data availability. The Lu–Hf and trace element dataset can be found at <https://doi.org/10.25909/17425541.v1> (Simpson, 2021).

Author contributions. AS contributed the following: conceptualisation, method development, experimentation, and paper drafting. StG contributed the following: conceptualisation, paper drafting, and primary supervision. MH contributed the following: conceptualisation, paper drafting, and secondary supervision. CS contributed the following: conceptualisation, sampling, and paper drafting. SaG contributed the following: method development, experimentation, and paper drafting. BC contributed the following: experimentation and paper drafting.

Competing interests. The contact author has declared that neither they nor their co-authors have any competing interests.

Disclaimer. Publisher's note: Copernicus Publications remains neutral with regard to jurisdictional claims in published maps and institutional affiliations.

Acknowledgements. The authors would like to thank the MinEx CRC for funding this research. The initial method development and apatite dating were supported by the Australian Research Council. Morgan Blades is thanked for supplying a sample of Otter Lake calcite. Anthony Milnes from the Tate Museum at the University of Adelaide is acknowledged for help during sampling and Aoife McFadden is acknowledged for assistance in operating the SEM at Adelaide Microscopy. Nick Roberts and Donald Davis are thanked for constructive comments during review.

Financial support. This research has been supported by the Australian Research Council (grant no. DP200101881).

Review statement. This paper was edited by Sandra Kamo and reviewed by Nick Roberts and Donald Davis.

References

Barfod, G. H., Krogstad, E. J., Frei, R., and Albarède, F.: Lu–Hf and PbSL geochronology of apatites from Proterozoic terranes: A first look at Lu–Hf isotopic closure in metamorphic apatite, *Geochim. Cosmochim. Ac.*, 69, 1847–1859, <https://doi.org/10.1016/j.gca.2004.09.014>, 2005.

Barker, S. L. L., Bennett, V. C., Cox, S. F., Norman, M. D., and Gagan, M. K.: Sm–Nd, Sr, C and O isotope systematics in hydrothermal calcite–fluorite veins: Implications for fluid–rock reaction and geochronology, *Chem. Geol.*, 268, 58–66, <https://doi.org/10.1016/j.chemgeo.2009.07.009>, 2009.

Basson, I., Lourens, P., Paetzold, H.-D., Thomas, S., Brazier, R., and Molabe, P.: Structural analysis and 3D modelling of major min-

eralizing structures at the Phalaborwa copper deposit, *Ore Geol. Rev.*, 83, 30–42, 2017.

Brugger, J., Liu, W., Etschmann, B., Mei, Y., Sherman, D. M., and Testemale, D.: A review of the coordination chemistry of hydrothermal systems, or do coordination changes make ore deposits?, *Chem. Geol.*, 447, 219–253, <https://doi.org/10.1016/j.chemgeo.2016.10.021>, 2016.

Cherniak, D. J.: An experimental study of strontium and lead diffusion in calcite, and implications for carbonate diagenesis and metamorphism, *Geochim. Cosmochim. Ac.*, 61, 4173–4179, [https://doi.org/10.1016/S0016-7037\(97\)00236-6](https://doi.org/10.1016/S0016-7037(97)00236-6), 1997.

Chew, D. M., Sylvester, P. J., and Tubrett, M. N.: U–Pb and Th–Pb dating of apatite by LA-ICPMS, *Chem. Geol.*, 280, 200–216, <https://doi.org/10.1016/j.chemgeo.2010.11.010>, 2011.

Cosca, M. A., Essene, E. J., Mezger, K., and van der Pluijm, B. A.: Constraints on the duration of tectonic processes: Protracted extension and deep-crustal rotation in the Grenville orogen, *Geology*, 23, 361–364, 1995.

Debruyne, D., Hulsbosch, N., and Muchez, P.: Unraveling rare earth element signatures in hydrothermal carbonate minerals using a source–sink system, *Ore Geol. Rev.*, 72, 232–252, <https://doi.org/10.1016/j.oregeorev.2015.07.022>, 2016.

Duncan, R. J., Stein, H. J., Evans, K. A., Hitzman, M. W., Nelson, E. P., and Kirwin, D. J.: A New Geochronological Framework for Mineralization and Alteration in the Selwyn-Mount Dore Corridor, Eastern Fold Belt, Mount Isa Inlier, Australia: Genetic Implications for Iron Oxide Copper-Gold Deposits, *Econ. Geol.*, 106, 169–192, 2011.

Elzinga, E. J., Reeder, R. J., Withers, S. H., Peale, R. E., Mason, R. A., Beck, K. M., and Hess, W. P.: EXAFS study of rare-earth element coordination in calcite, *Geochim. Cosmochim. Ac.*, 66, 2875–2885, [https://doi.org/10.1016/S0016-7037\(02\)00888-8](https://doi.org/10.1016/S0016-7037(02)00888-8), 2002.

Fisher, C. M. and Vervoort, J. D.: Using the magmatic record to constrain the growth of continental crust – The Eoarchean zircon Hf record of Greenland, *Earth Planet. Sc. Lett.*, 488, 79–91, <https://doi.org/10.1016/j.epsl.2018.01.031>, 2018.

Frei, R., Villa, I. M., Nagler, T. F., Kramers, J. D., Pryzbylowicz, W. J., Prozesky, V. M., Hofman, B. A., and Kamber, B. S.: Single mineral dating by the Pb–Pb step leaching method: assessing the mechanisms, *Geochim. Cosmochim. Ac.*, 61, 393–414, 1997.

Garrett, S. J.: The Geology and Geochemistry of the Mount Elliott Copper-Gold deposit, Northwest Queensland, Masters thesis, CODES, University of Tasmania, Tasmania, 139 pp., <https://eprints.utas.edu.au/19572/> (last access: 8 December 2021), 1992.

Gibson, H. L., Lafrance, B., Pehrsson, S., Dewolfe, M. Y., Gilmore, K., and Simard, R.-L.: The Volcanological and Structural Evolution of the Paleoproterozoic Flin Flon Mining District, Anatomy of a Giant VMS System, *Geosci. Can.*, 39, 182–194, 2012.

Giles, D. and Nutman, A. P.: SHRIMP U–Pb monazite dating of 1600–1580 Ma amphibolite facies metamorphism in the southeastern Mt. Isa Block, Australia, *Aust. J. Earth Sci.*, 49, 455–465, <https://doi.org/10.1046/j.1440-0952.2002.00931.x>, 2002.

Glorie, S., Gillespie, J., Simpson, A., Gilbert, S., Khudoley, A., Priyatkina, N., Hand, M., and Kirkland, C. L.: Detrital apatite Lu–Hf and U–Pb geochronology applied to the southwestern Siberian margin, *Terra Nova*, 34, 201–209, <https://doi.org/10.1111/ter.12580>, 2022.

- Groves, D. I. and Vielreicher, N. M.: The Phalaborwa (palabora) carbonatite-hosted magnetite-copper sulfide deposit, South Africa: an emd-member of the iron-oxide-copper-gold-rare earth element deposit group?, *Miner. Deposita*, 36, 189–194, 2001.
- Henrichs, I. A., O’Sullivan, G., Chew, D. M., Mark, C., Babechuk, M. G., McKenna, C., and Emo, R.: The trace element and U-Pb systematics of metamorphic apatite, *Chem. Geol.*, 483, 218–238, <https://doi.org/10.1016/j.chemgeo.2017.12.031>, 2018.
- Horstwood, M. S. A., Košler, J., Gehrels, G., Jackson, S. E., McLean, N. M., Paton, C., Pearson, N. J., Sircombe, K., Sylvester, P., Vermeesch, P., Bowring, J. F., Condon, D. J., and Schoene, B.: Community-Derived Standards for LA-ICP-MS U-(Th)-Pb Geochronology – Uncertainty Propagation, Age Interpretation and Data Reporting, *Geostand. Geoanal. Res.*, 40, 311–332, <https://doi.org/10.1111/j.1751-908X.2016.00379.x>, 2016.
- Hu, Z., Gao, S., Liu, Y., Hu, S., Chen, H., and Yuan, H.: Signal enhancement in laser ablation ICP-MS by addition of nitrogen in the central channel gas, *J. Anal. Atom. Spectrom.*, 23, 1093–1101, <https://doi.org/10.1039/b804760j>, 2008.
- Kennedy, A. K., Kamo, S. L., Nasdala, L., and Timms, N. E.: Grenville Skarn Titanite: Potential Reference Material For Sims U-Th-Pb Analysis, *Can. Mineral.*, 48, 1423–1443, <https://doi.org/10.3749/canmin.48.5.1423>, 2011.
- Koo, J. and Mossman, D. J.: Origin and metamorphism of the Flin Flon stratabound Cu-Zn sulfide deposit, Saskatchewan and Manitoba, *Econ. Geol.*, 70, 48–62, 1975.
- Kretz, R., Campbell, J. L., Hoffman, E. L., Hartree, R., and Teesdale, W. J.: Approaches to equilibrium in the distribution of trace elements among the principal minerals in a high-grade metamorphic terrane, *J. Metamorph. Geol.*, 8, 493–506, 1999.
- Krogstad, R. and Walker, R. J.: High closure temperatures of the U-Pb system in large apatites from the Tin Mountain pegmatite, Black Hills South Dakota, USA, *Geochem. Geophys. Geos.*, 58, 3845–3853, 1994.
- Kroslovskaya, I. and Günther, D.: Elemental fractionation in laser ablation-inductively coupled plasma-mass spectrometry: evidence for mass load induced matrix effects in the ICP during ablation of a silicate glass, *J. Anal. Atom. Spectrom.*, 22, 51–62, <https://doi.org/10.1039/b606522h>, 2007.
- Lafrance, B., Gibson, H. L., Pehrsson, S., Schetselaar, E., Dewolfe, M. Y., and Lewis, D.: Structural reconstruction of the Flin Flon volcanogenic massive sulfide mining district, Saskatchewan and Manitoba, Canada, *Econ. Geol.*, 111, 849–875, 2016.
- Le Bras, L. Y., Bolhar, R., Bybee, G. M., Nex, P. A., Guy, B. M., Moyana, T., and Lourens, P.: Platinum-group and trace elements in Cu-sulfides from the Loolekop pipe, Phalaborwa: implications for ore-forming processes, *Miner. Deposita*, 56, 161–177, 2021.
- Li, Q., Parrish, R. R., Horstwood, M. S. A., and McArthur, J. M.: U-Pb dating of cements in Mesozoic ammonites, *Chem. Geol.*, 376, 76–83, <https://doi.org/10.1016/j.chemgeo.2014.03.020>, 2014.
- Li, Y. and Vermeesch, P.: Short communication: Inverse isochron regression for Re–Os, K–Ca and other chronometers, *Geochronology*, 3, 415–420, <https://doi.org/10.5194/gchron-3-415-2021>, 2021.
- Maas, R., Apukhtina, O. B., Kamenetsky, V. S., Ehrig, K., Sprung, P., and Münker, C.: Carbonates at the supergiant Olympic Dam Cu-U-Au-Ag deposit, South Australia part 2: Sm-Nd, Lu-Hf and Sr-Pb isotope constraints on the chronology of carbonate deposition, *Ore Geol. Rev.*, 140, 103745, <https://doi.org/10.1016/j.oregeorev.2020.103745>, 2020.
- Marshall, L.: Brecciation within the Mary Kathleen Group of the Eastern Succession, Mt. Isa Block, Australia: Implications of district-scale structural and metasomatic processes for Fe-oxide-Cu-Au mineralisation, PhD thesis, James Cook University, <https://researchonline.jcu.edu.au/8243/> (last access: 13 December 2021), 2003.
- Migdisov, A., Williams-Jones, A. E., Brugger, J., and Caporuscio, F. A.: Hydrothermal transport, deposition, and fractionation of the REE: Experimental data and thermodynamic calculations, *Chem. Geol.*, 439, 13–42, <https://doi.org/10.1016/j.chemgeo.2016.06.005>, 2016.
- Nebel, O., Morel, M., and Vroon, P.: Isotope Dilution Determinations of Lu, Hf, Zr, Ta and W and Hf Isotope Compositions of NIST SRM 610 and 612 Glass Wafers, *Geostand. Geoanal. Res.*, 33, 487–499, 2009.
- Nie, F. J., Bjørlykke, A., and Nilsen, K. S.: The Origin of the Proterozoic Bidjovagge Gold-Copper Deposit, Finnmark, Northern Norway, as Deduced from Rare Earth Element and Nd Isotopic Evidences on Calcites, *Resour. Geol.*, 49, 13–25, <https://doi.org/10.1111/j.1751-3928.1999.tb00028.x>, 1999.
- Norris, A. and Danyushevsky, L.: Towards estimating the complete uncertainty budget of quantified results measured by LA-ICP-MS, *Goldschmidt*, 12–17 August 2018, Boston, USA, 1894, <https://goldschmidtabstracts.info/2018/1894.pdf> (last access: December 2021), 2018.
- Oliver, N., Butera, K., Rubenach, M., Marshall, L., Cleverley, J., Mark, G., Tullemans, F., and Esser, D.: The protracted hydrothermal evolution of the Mount Isa Eastern Succession: A review and tectonic implications, *Precambrian Res.*, 163, 108–130, <https://doi.org/10.1016/j.precamres.2007.08.019>, 2008.
- Oliver, N. H., Cartwright, I., Wall, V. J., and Golding, S. D.: The stable isotope signature of kilometre-scale fracturedominated metamorphic fluid pathways, Mary Kathleen, Australia, *J. Metamorph. Geol.*, 11, 705–720, <https://doi.org/10.1111/j.1525-1314.1993.tb00182.x>, 1993.
- Oliver, N. H., Cleverley, J. S., Mark, G., Pollard, P. J., Fu, B., Marshall, L. J., Rubenach, M. J., Williams, P. J., and Baker, T.: Modeling the Role of Sodic Alteration in the Genesis of Iron Oxide-Copper-Gold Deposits, Eastern Mount Isa Block, Australia, *Econ. Geol.*, 99, 1145–1176, <https://doi.org/10.2113/gsecongeo.99.6.1145>, 2004.
- Page, R. W. and Sun, S. S.: Aspects of geochronology and crustal evolution in the Eastern Fold Belt, Mt. Isa Inlier, Aust. *J. Earth Sci.*, 45, 343–361, <https://doi.org/10.1080/08120099808728396>, 1998.
- Peng, J. T., Hu, R. Z., and Burnard, P. G.: Samarium-neodymium isotope systematics of hydrothermal calcites from the Xikuangshan antimony deposit (Hunan, China): the potential of calcite as a geochronometer, *Chem. Geol.*, 200, 129–136, [https://doi.org/10.1016/S0009-2541\(03\)00187-6](https://doi.org/10.1016/S0009-2541(03)00187-6), 2003.
- Rasbury, E. T. and Cole, J. M.: Directly dating geologic events: U-Pb dating of carbonates, *Rev. Geophys.*, 47, RG3001, <https://doi.org/10.1029/2007RG000246>, 2009.
- Rayner, N. M.: New U-Pb zircon ages from the Flin Flon Targeted Geoscience Initiative Project 2006–2009: Flin Flon and Hook Lake blocks, Geological Survey of Canada, Current Research, 2010-4, 1–12, <https://doi.org/10.4095/261489>, 2010.

- Ribeiro, B. V., Finch, M. A., Cawood, P. A., Faleiros, F. M., Murphy, T. D., Simpson, A., Glorie, S., Tedeschi, M., Armit, R., and Barrote, V. R.: From microanalysis to supercontinents: insights from the Rio Apa Terrane into the Mesoproterozoic SW Amazonian Craton evolution during Rodinia assembly, *J. Metamorph. Geol.*, 40, 631–663, <https://doi.org/10.1111/jmg.12641>, 2021.
- Ring, U. and Gerdes, A.: Kinematics of the Alpenrhein-Bodensee graben system in the Central Alps: Oligocene/Miocene transtension due to formation of the Western Alps arc, *Tectonics*, 35, 1367–1391, <https://doi.org/10.1002/2015tc004085>, 2016.
- Rivers, T.: Tectonic Setting and Evolution of the Grenville Orogen: An Assessment of Progress Over the Last 40 Years, *Geosci. Can.*, 42, 77–124, <https://doi.org/10.12789/geocanj.2014.41.057>, 2015.
- Roberts, N. M. W. and Walker, R. J.: U–Pb geochronology of calcite-mineralized faults: Absolute timing of rift-related fault events on the northeast Atlantic margin, *Geology*, 44, 531–534, <https://doi.org/10.1130/G37868.1>, 2016.
- Roberts, N. M. W., Rasbury, E. T., Parrish, R. R., Smith, C. J., Horstwood, M. S. A., and Condon, D. J.: A calcite reference material for LA-ICP-MS U–Pb geochronology, *Geochem. Geophys. Geos.*, 18, 2807–2814, <https://doi.org/10.1002/2016GC006784>, 2017.
- Roberts, N. M. W., Drost, K., Horstwood, M. S. A., Condon, D. J., Chew, D., Drake, H., Milodowski, A. E., McLean, N. M., Smye, A. J., Walker, R. J., Haslam, R., Hodson, K., Imber, J., Beaudoin, N., and Lee, J. K.: Laser ablation inductively coupled plasma mass spectrometry (LA-ICP-MS) U–Pb carbonate geochronology: strategies, progress, and limitations, *Geochronology*, 2, 33–61, <https://doi.org/10.5194/gchron-2-33-2020>, 2020.
- Schetselaar, E., Ames, D., and Grunsky, E.: Integrated 3D Geological Modeling to Gain Insight in the Effects of Hydrothermal Alteration on Post-Ore Deformation Style and Strain Localization in the Flin Flon Volcanogenic Massive Sulfide Ore System, *Minerals*, 8, 3, <https://doi.org/10.3390/min8010003>, 2017.
- Schneider, D. A., Heizler, M. T., Bickford, M. E., Wortman, G. L., Condie, K. C., and Perilli, S.: Timing constraints of orogeny to cratonization: Thermochronology of the Paleoproterozoic Trans-Hudson orogen, Manitoba and Saskatchewan, Canada, *Precambrian Res.*, 153, 65–95, <https://doi.org/10.1016/j.precamres.2006.11.007>, 2007.
- Schumann, D., Martin, R. F., Fuchs, S., and de Fourestier, J.: Silicocarbonatitic melt inclusions in fluorapatite from the Yates prospect, Otter Lake, Québec: Evidence of marble anatexis in the central metasedimentary belt of the Grenville Province, *Can. Mineral.*, 57, 583–604, <https://doi.org/10.3749/canmin.1900015>, 2019.
- Simpson, A.: Supplementary file 1: calcite Lu–Hf data, The University of Adelaide [data set], <https://doi.org/10.25909/17425541.v1>, 2021.
- Simpson, A., Gilbert, S., Tamblyn, R., Hand, M., Spandler, C., Gillespie, J., Nixon, A., and Glorie, S.: In-situ Lu Hf geochronology of garnet, apatite and xenotime by LA ICP MS/MS, *Chem. Geol.*, 577, 120299, <https://doi.org/10.1016/j.chemgeo.2021.120299>, 2021a.
- Simpson, A., Glorie, S., Morley, C. K., Roberts, N. M. W., Gillespie, J., and Lee, J. K.: In-situ calcite U–Pb geochronology of hydrothermal veins in Thailand: New constraints on Indosinian and Cenozoic deformation, *J. Asian Earth Sci.*, 206, 104649, <https://doi.org/10.1016/j.jseaes.2020.104649>, 2021b.
- Söderlund, U., Patchett, P. J., Vervoort, J. D., and Isachsen, C. E.: The ^{176}Lu decay constant determined by Lu–Hf and U–Pb isotope systematics of Precambrian mafic intrusions, *Earth Planet. Sc. Lett.*, 219, 311–324, [https://doi.org/10.1016/s0012-821x\(04\)00012-3](https://doi.org/10.1016/s0012-821x(04)00012-3), 2004.
- Spandler, C., Hammerli, J., Sha, P., Hilbert-Wolf, H., Hu, Y., Roberts, E., and Schmitz, M.: MKED1: A new titanite standard for in situ analysis of Sm–Nd isotopes and U–Pb geochronology, *Chem. Geol.*, 425, 110–126, <https://doi.org/10.1016/j.chemgeo.2016.01.002>, 2016.
- Staff, P. M.: The Geology and the economic deposits of copper, iron, and vermiculite in the Palabora Igneous Complex, A brief review, *Econ. Geol.*, 71, 177–192, 1976.
- Stern, R. A. and Amelin, Y.: Assessment of errors in SIMS zircon U–Pb geochronology using a natural zircon standard and NIST SRM 610 glass, *Chem. Geol.*, 197, 111–142, [https://doi.org/10.1016/s0009-2541\(02\)00320-0](https://doi.org/10.1016/s0009-2541(02)00320-0), 2003.
- Stern, R. A., Syme, E. C., Bailes, A. H., and Lucas, S. B.: Paleoproterozoic (1.90–1.86 Ga) arc volcanism in the Flin Flon Belt, Trans-Hudson Orogen, Canada, *Contrib. Mineral. Petr.*, 119, 117–141, <https://doi.org/10.1007/BF00307276>, 1995.
- Sylvester, P.: Matrix effects in laser ablation ICP–MS, in: *Laser Ablation–ICP–MS in the Earth Sciences current practices and outstanding issues*, edited by: Sylvester, P., Mineralogical Association of Canada short course series, Mineralogical Association of Canada, Vancouver, <https://doi.org/10.2113/gsecongeo.104.4.601>, 2008.
- Tamblyn, R., Hand, M., Simpson, A., Gilbert, S., Wade, B., and Glorie, S.: In-situ laser ablation Lu–Hf geochronology of garnet across the Western Gneiss Region: Campaign-style dating of metamorphism, *J. Geol. Soc.*, jgs2021-2094, <https://doi.org/10.1144/jgs2021-094>, online first, 2021.
- Terakado, Y. and Masuda, A.: The coprecipitation of rare-earth elements with calcite and aragonite, *Chem. Geol.*, 69, 103–110, [https://doi.org/10.1016/0009-2541\(88\)90162-3](https://doi.org/10.1016/0009-2541(88)90162-3), 1988.
- van Breemen, O. v. and Corriveau, L.: U–Pb age constraints on arenaceous and volcanic rocks of the Wakeham Group, eastern Grenville Province, *Can. J. Earth Sci.*, 42, 1677–1697, <https://doi.org/10.1139/e05-079>, 2005.
- Vermeesch, P.: IsoplotR: A free and open toolbox for geochronology, *Geosci. Front.*, 9, 1479–1493, <https://doi.org/10.1016/j.gsf.2018.04.001>, 2018.
- Vervoort J.: Lu–Hf Dating: The Lu–Hf Isotope System, in: *Encyclopedia of Scientific Dating Methods*, edited by: Rink, W. and Thompson, J., Springer, Dordrecht, https://doi.org/10.1007/978-94-007-6326-5_46-1, 2014.
- Wang, S. and Williams, P. J.: Geochemistry and origin of Proterozoic skarns at the Mount Elliott Cu–Au(–Co–Ni) deposit, Cloncurry district, NW Queensland, Australia, *Miner. Deposita*, 36, 109–124, 2001.
- Whitehouse, M. J. and Russell, J.: Isotope systematics of Precambrian marbles from the Lewisian complex of northwest Scotland: implications for Pb–Pb dating of metamorphosed carbonates, *Chem. Geol.*, 136, 295–307, [https://doi.org/10.1016/S0009-2541\(96\)00137-4](https://doi.org/10.1016/S0009-2541(96)00137-4), 1997.
- Wu, F.-Y., Yang, Y.-H., Li, Q.-L., Mitchell, R. H., Dawson, J. B., Brandl, G., and Yuhara, M.: In situ determination of U–Pb

- ages and Sr–Nd–Hf isotopic constraints on the petrogenesis of the Phalaborwa carbonatite Complex, South Africa, *Lithos*, 127, 309–322, <https://doi.org/10.1016/j.lithos.2011.09.005>, 2011.
- Xiang, D., Zhang, Z., Zack, T., Chew, D., Yang, Y., Wu, L., and Hogmalm, J.: Apatite U–Pb Dating with Common Pb Correction Using LA-ICP-MS/MS, *Geostand. Geoanal. Res.*, 45, 621–642, <https://doi.org/10.1111/ggr.12404>, 2021.
- Zhong, S. and Mucci, A.: Partitioning of rare earth elements (REEs) between calcite and seawater solutions at 25 °C and 1 atm, and high dissolved REE concentrations, *Geochim. Cosmochim. Ac.*, 59, 443–453, [https://doi.org/10.1016/0016-7037\(94\)00381-U](https://doi.org/10.1016/0016-7037(94)00381-U), 1995.